A scanning echelle monochromator for ICP-OES with dynamic wavelength stabilization and CCD detection

JAAS

Full Paper

Helmut Becker-Ross,[a] Stefan Florek,[a] Helmut Franken,[b] Bernard Radziuk*[b] and Michael Zeiher[b]

[a]*Institut für Spektrochemie und angewandte Spektroskopie, Institutsteil Berlin, Albert-Einstein-Str. 9, D-12489 Berlin-Adlershof, Germany*
[b]*Perkin Elmer Bodenseewerk, Alte Nußdorter Str. 21, D-88662 Überlingen, Germany. E-mail: Bernard_Radziuk@eur.perkin-elmer.com*

Received 8th February 2000, Accepted 27th April 2000
Published on the Web 9th June 2000

The design and evaluation of a scanning spectrometer with CCD detection are described. The spectrometer is a double monochromator employing a CaF_2 prism to pre-select a spectral region equivalent to a single order for admission into an echelle grating monochromator. This design makes possible unambiguous wavelength selection without a restriction in entrance slit height. All wavelengths between 165 and 900 nm can be accessed by rotation of the dispersing elements within a range of $\pm 2.4°$. A novel approach is taken to provide dynamic wavelength stabilization based on the simultaneous measurement of a neon reference spectrum. A dual back illuminated CCD was custom designed to match the characteristics of the spectrometer, provide for the simultaneous measurement of background in the vicinity of the analyte line and to facilitate the measurement of the reference spectrum. The detector exhibits a quantum efficiency greater than 50% throughout the UV range and a very low specific dark current so that cooling to $-8\,°C$ is sufficient for ICP-OES applications. This temperature is maintained by means of an integrated single stage Peltier cooling element. The spectrometer has a measured spectral bandpass of 0.007 nm at 200 nm. The dual monochromator design results in very low levels of diffuse stray light: with axial viewing in an ICP, a 10 000 mg L^{-1} Ca solution causes a shift in baseline at 193.696 nm equivalent to the peak height measured for a solution containing 75 μg L^{-1} As. The dynamic approach to wavelength stabilization is demonstrated to function effectively over a wide ambient temperature range. As a result, measured spectral line intensity was stable to within $\pm 2\%$ over a period of several days during which ambient temperature was varied cyclically between 15 and 35 °C. The analytical performance in both axial and radial viewing modes is in keeping with the design and is limited by plasma background shot noise when simultaneous background correction is used. The high geometric radiation throughput provides for high measurement quality in short integration times. With axial viewing of the plasma and 5 s integration time, 3σ detection limits measured for P (177.434 nm), Tl (190.801 nm) and Se (196.026 nm) using a cross-flow nebulizer were 3.0, 2.2 and 2.7 μg L^{-1}, respectively.

The first systematic studies on quantitative measurement by optical emission spectrometry (OES) were made using a spark for excitation and a photographic plate for registration of intensity.[1–3] Over the years, this method of detection was matched to ever more sophisticated spectrometers and, for a considerable period, the combination of a long focal length spectrograph with photographic detection represented the state of the art for OES, providing complete spectral information at high resolution. Photomultiplier tubes (PMT) made direct electronic registration possible which increased sensitivity while simplifying the process of quantification but at the cost of most of the spectral information available from the spectrometer. A typical 'direct reading' spectrometer was based on a concave grating with a large number of photomultipliers placed behind slits at appropriate points on the Rowland circle.[4] Mechanical considerations did sometimes limit the accessible locations. Since each PMT measured the radiation from a very narrow spectral range only, background correction was done sequentially by moving the entrance slit stepwise or a by means of a refractor plate.

With the advent of the ICP, a source producing a steady state signal of any desired duration became available. It was now practicable to perform multielement determinations by simultaneously or sequentially measuring intensities at different points of the spectrum. A significant advantage of the latter was that any desired wavelength could be accessed, but the total measurement time was the sum of not only all individual measurement times but also all wavelength slewing times. In addition, the grating itself would often be used to sequentially scan the vicinity of the peak in order to measure spectral background.

The characteristics of simultaneously and sequentially measuring spectrometers are complementary and some manufacturers went so far as to include both a mono- and a polychromator in a single instrument. A unique 'field-programmable direct reader' combining a dispersion–selection–recombination line selector with a linear photodiode array[5] pioneered the application of solid state detection to ICP-OES. In recent years, the combination of echelle polychromators producing 2-dimensional spectra with multichannel solid state detectors has enhanced the flexibility while maintaining the performance of PMT based systems.[6–8] A major advantage of the use of solid state detectors has proven to be the ability to measure analyte emission and spectral background simultaneously in analogy to photographic film, but with all the advantages of photoelectric registration. This not only increases sample throughput further, but also provides a marked improvement in precision since the contribution of source flicker components to the analytical signal is eliminated. Well-designed systems can meet the major requirements of OES, such as high resolving power, high optical throughput, extensive spectral coverage and good wavelength stability.

There are, however, inevitable compromises still associated with echelle-based, simultaneously measuring spectrometers. Dispersion in two directions coupled with physical and cost limitations on detector dimensions generally limits geometrical slit dimensions, *i.e.*, height, and, therefore, optical throughput. Moreover, it is difficult to achieve constant image quality over the entire surface of a large, two-dimensional focal plane. Some of these limitations have been circumvented elegantly, though with a significant increase in complexity, by dividing the spectrum into separate output regions for the UV and visible ranges and by demagnification.[7] Another consideration is that the plasma conditions (power, viewing position, flow rates) are not identical for all elements and so either compromised conditions are used or a suite of elements will often be subdivided into groups measured in sequence.

Currently available sequentially measuring spectrometers are based on conventional monochromators equipped with one or more photomultiplier tubes as detectors. Typically, holographically produced gratings with 1800 or more lines per mm are employed in the 1st to 4th orders.[9] Focal lengths required to achieve a spectral bandpass of approximately 6 pm are of the order of 700 to 1000 cm.

The advantages of an echelle grating (*i.e.*, high dispersion, blaze at all wavelengths) can also be applied to a sequentially measuring spectrometer system. In the past, echelle polychromators have been used as a monochromator by adjusting the positions of grating and prism.[10] More advantageously, a separate monochromator can be placed before the echelle monochromator for the purpose of removing ambiguities due to order overlap.[11] Thus, there is no longer a restriction on the height of the entrance slit for the echelle monochromator, and the increase in throughput is limited only by the source characteristics and optical aberrations. Only a narrow spectral range enters the echelle grating monochromator, so that only this range rather than the entire spectrum can contribute to the level of diffuse stray light at the detector. Coverage of the wavelength range between 165 and 900 nm can be accomplished by rotation of the prism and grating through only a few degrees, dramatically increasing the speed of wavelength selection. The image quality is constant over the entire spectral range and the high dispersion of the echelle grating results in a compact, high resolution, intrinsically stable spectrometer. Alternatively the design principle can be used to construct long focal length monochromators which operate at very high resolution for use in fundamental studies.[12–14]

The high information density available in the spectrum of an ICP has the drawback that there is a high probability of spectral interference. Mathematical methods have been developed which greatly improve the correction for complex background.[15] These rely on exact and stable assignment of intensities to wavelengths. Accurate and reproducible analysis by ICP-OES requires therefore not only adequate spectral resolution but also excellent wavelength stability. In polychromators with no moving parts, causes of wavelength drift are largely thermal but shifts can also arise due to changes in barometric pressure. In monochromators, the precision of the wavelength selecting action is an additional factor. In general, precise thermostating and periodic recalibration using a reference source have been essential to the achievement of acceptable wavelength stability. An attractive alternative would be to use a continuously available reference spectrum in order to compensate actively for drifts and mechanical tolerances.

In this work, a spectrometer system for ICP-OES with dynamic wavelength stabilization consisting of a back illuminated CCD (Charge Coupled Device) detector matched to a scanning echelle monochromator with order pre-selection was designed and evaluated. The detector provides high UV quantum efficiency and makes possible the simultaneous measurement of analyte and background spectra as well as of a reference spectrum.

Experimental

Design considerations

According to the signal-to-background ratio–relative standard deviation of the background (SBR-RSDB) method of Boumans,[16] detection limits in ICP-OES can be calculated as:

$$\mathrm{LOD} = 3 \times \mathrm{RSDB} \times \mathrm{BEC} \quad (1)$$

where RSDB is calculated by combining the variances of the noise sources which determine the relative standard deviation of the background:

$$\mathrm{RSDB} = (\alpha^2 + 1/z_b\tau(1 + z_d/z_b + {\sigma_{ro}}^2/z_b\tau))^{1/2} \quad (2)$$

and BEC, the background equivalent concentration, is the solution concentration of analyte producing a net intensity equal to the intensity measured for the plasma background alone. In eqn. (2), α is the flicker noise parameter, z_b is the spectral background, z_d is the detector dark current, z_{ro} is the standard deviation of readout noise and τ is the integration time of the measurement.

The key parameters determining the detection limit performance of an optics-detector system for ICP-OES can be inferred from the above. Performance can be improved by reducing BEC and/or RSDB. Background equivalent concentration depends directly on spectral bandpass and the level of diffuse stray light. Spectral bandpass is determined by the combined effect of dispersion and image quality, whereas stray light depends on both spectrometer design and component quality.

Flicker noise is intrinsic to the source, but has been shown to be wavelength-correlated so that it can be minimized by simultaneous background measurement.[17] Under these conditions, RSDB depends directly on the combination of detector dark current and read out noise variances with plasma background shot noise variance in the pixels used for both peak and background correction measurements. In the spectral regions where plasma background shot noise predominates, the expression for RSDB reduces to

$$\mathrm{RSDB} = (1/z_b\tau)^{1/2} \quad (3)$$

and the total integration time required to obtain a given detection limit is inversely proportional to the number of photoelectrons generated by the plasma background in the detector per unit time. This in turn depends on the optical throughput of the spectrometer and the quantum efficiency of the detector. As wavelength decreases, the plasma background decreases and the detection limit eventually becomes dependent also on the ratio between the charge generated per unit time by detector dark current and by plasma background photons.

Thus, the design goals for an ICP spectrometer are low spectral bandpass and stray light level, and simultaneous measurement of background and analyte line intensity using a detector with noise characteristics, which allow plasma spectral background to dominate over as much of the spectrum as possible. In practice, when samples are to be analyzed for multiple elements, the overall measurement time required to achieve a given quality depends also on factors such as the extent to which plasma conditions must be varied for different elements and on the speed and accuracy of wavelength selection.

Optical system

The optical system consists of an image transfer section designed for viewing the plasma either axially or radially and

two sequentially configured dispersive sections. The first of the dispersive sections makes use of a prism and the second of an echelle grating. The spectrum of a neon reference lamp is coupled directly to the intermediate slit between the two dispersive sections by means of an optical fiber. In order to make sensitive measurements at VUV wavelengths possible, the entire optics are mounted in a cast aluminum tub which is sealed for efficient purging with inert gas. The purge gas flows through an extension mounted on the tub and protruding into the sample compartment. The extension is designed to minimize the air path in both viewing modes and is sealed by means of fused silica windows. The overall layout of the optical system is shown in Fig. 1, while the specifications of important components are summarized in Table 1.

For axial viewing, the plasma analyte channel is imaged one to one by a toroidal mirror onto the 3 mm high entrance slit of the prism monochromator. The beam is folded onto a fine guiding mirror which can be translated horizontally and vertically under stepper motor control in order to scan the plasma image across the slit and make possible automatic selection of the optimum viewing zone. The resolution of the image translation is 0.095 mm per step in the vertical, and 0.045 mm per step in the horizontal direction. In radial viewing mode, a second toroid is moved into the beam using a stepper motor and spring mechanism designed to select between one of two mechanical stops assuring reproducible positioning. In combination with a plane mirror located in the cast aluminum arm under the plasma, this allows viewing of the torch from below. In this case, the image of the plasma is demagnified by a factor of 1.7 at the entrance slit so that a 5 mm region along the plasma axis is viewed, reducing the effects of aerosol noise and optimizing the spatial profile. The same fine guiding mirror as for axial viewing is used for scanning the radial view with, in this case, resolution of 0.15 and 0.08 mm per motor step along the plasma axis and orthogonally to it, respectively. A shutter wheel is mounted on the transfer optics module. The wheel can be positioned by stepper motor in order to allow either radial or axial beams or no beam at all to enter the main body of the spectrometer. In addition, a grid can be placed in the beam at locations such that either the axial or the radial beam is attenuated by a factor of 50.

As in typical echelle polychromators, use is made in the present system of the fundamental property of an echelle grating, that it can be used at large angles of incidence and diffraction, which results in high angular dispersion.[18,19] The relationship between incident and diffracted beams at the grating is described by the grating equation

$$m\lambda = d(\sin\ \alpha + \sin\ \beta) \tag{4}$$

with m the order number, λ the wavelength, d the grating constant (the groove spacing) and α and β the angles of incidence and diffraction referred to the grating normal, respectively.

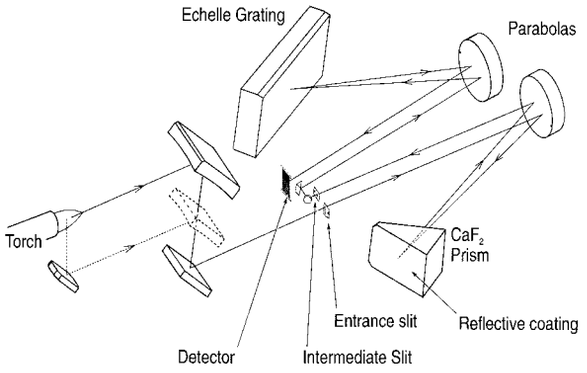

Fig. 1 Schematic diagram of the optical system. The dashed line indicates the path for radial viewing of the plasma from underneath.

Table 1 Optical component specifications

Entrance slits—	
Height	3000 μm
Widths	300 μm, 150 μm
Intermediate slit—	
Height	3000 μm + 500 μm
Width	30 μm
Littrow mirrors—	
Optical figure	10° off-axis parabola
Focal length	300 mm
Aperture diameter	55 mm
Reflecting prism—	
Apex angle	30°
Material	Calcium fluoride
Echelle grating—	
Groove frequency	79.0 lines mm^{-1}
Blaze angle	63.8°
Dimensions	60 × 140 mm
Optical fiber—	
Diameter	0.5 mm

Echelle gratings are characterized generally by the situation, that $d \gg \lambda$ and $m \gg 1$. The relatively large grooves are shaped like stair steps resulting in a strong blaze effect, which is characterized by the blaze angle θ_B. To obtain maximum diffraction energy, the echelle grating is used close to autocollimation near the blaze angle, *i.e.*, with

$$\alpha \approx \beta \approx \theta_B \tag{5}$$

Under these conditions, the central wavelength for each order m is defined by the grating equation as

$$\lambda = 2d\ \sin\ \theta_B/m \tag{6}$$

Conversely, the order containing the highest energy for a given wavelength λ corresponds to

$$m = 2d\ \sin\ \theta_B/\lambda \tag{7}$$

The wavelength width of a given order m, also called the free spectral range, $\Delta\lambda$, is given by differentiation of the grating equation

$$\Delta\lambda = \lambda/m \tag{8}$$

Similarly, the angular dispersion $d\beta/d\lambda$ is derived from the differentiated grating equation and gives, for the blaze maximum wavelength,

$$d\beta/d\lambda = 2\ \tan\ \theta_B/\lambda \tag{9}$$

The angle of diffraction at which any wavelength is to be measured while fulfilling the blaze condition is calculated according to

$$\beta(\lambda, m) = \arcsin(m\lambda/d - \sin\ \alpha) \tag{10}$$

and, when plotted against wavelength, follows a saw tooth pattern about the blaze angle as shown in Fig. 2. It is apparent from the figure that many wavelengths are diffracted at any given angle. In order to permit unambiguous measurement of intensity at a selected wavelength, the diffracted beam can be passed through a second dispersive element mounted so that the direction of dispersion is orthogonal to that of echelle diffraction. This results in the familiar two dimensional pattern, similar in form to Fig. 2, at the exit plane of echelle polychromators.[10]

In the present system, a pre-disperser arranged with slits parallel to that of the echelle monochromator is set to transmit a wavelength range corresponding to the order containing the selected wavelength. More precisely, the function of the first monochromator is to guarantee that no radiation from

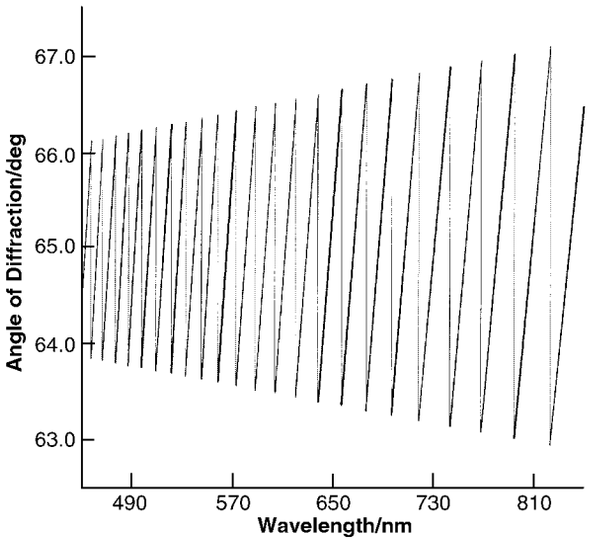

Fig. 2 Plot of angle of diffraction as a function of wavelength for the 79 line mm^{-1}, 63.8° blaze grating used in this work.

adjacent orders reaches the detector for any given grating position. Since this wavelength range varies with order, as can be inferred from Fig. 2, the pre-disperser must operate with variable spectral bandpass. The order widths corresponding to the wavelength extremes required for ICP-OES are 1.2 nm at 167 nm and 31.2 nm at 850 nm. The very small order width at short wavelengths mandates the use of a device with dispersion which increases with decreasing wavelength. This is typical of a prism monochromator. The angle of incidence and refraction in autocollimation mode is given by

$$\varepsilon(\lambda) = \arcsin\,[n(\lambda)\,\sin\,(\gamma)] \qquad (11)$$

where $n(\lambda)$ is the index of refraction of calcium fluoride and γ is the apex angle of the prism. Since $n(\lambda)$ increases dramatically below 400 nm, the angular dispersion resulting from differentiation of this expression is such that, for a 300 mm focal length and 300 μm entrance slit, the spectral bandpass is 0.3 nm at 167 nm and 75 nm at 850 nm. Thus a configuration transmitting less than one order width at very short wavelengths will result in the overlap of several orders at the long wavelength extreme. Selection of a slit width preventing overlap at the longer wavelengths results in transmission of a bandpass in the UV which is smaller than the wavelength range of interest.

Ideally, the characteristics of the pre-disperser would be continuously matched to the echelle spectrum throughout the wavelength range. This can be elegantly accomplished by means of a prism with continuously variable apex angle. One such design has been demonstrated using a prism constructed from two hinged plates joined by a water filled bellows.[20] However, a good compromise can be made by using an entrance slit 300 μm wide for wavelengths below about 460 nm and a slit 150 μm wide for longer wavelengths. Using this combination, there is uniform illumination for 0.24 nm at 167 nm in order 136 and the wavelengths falling within a 60 pixel measurement range are unambiguously pre-selected in all orders down to and including order 23 with central wavelength 967 nm.

The resolving power of a grating approaches the theoretical maximum when the grating is used in autocollimation, *i.e.*, the incident propagation vector is almost normal to the groove face and angles of incidence and diffraction are equal and on the same side of the grating normal. Both monochromators use Littrow autocollimation mounts[21] with identical 10° off-axis parabolas. Thus spherical aberration, coma and astigmatism are avoided, resulting in good image quality over the entire

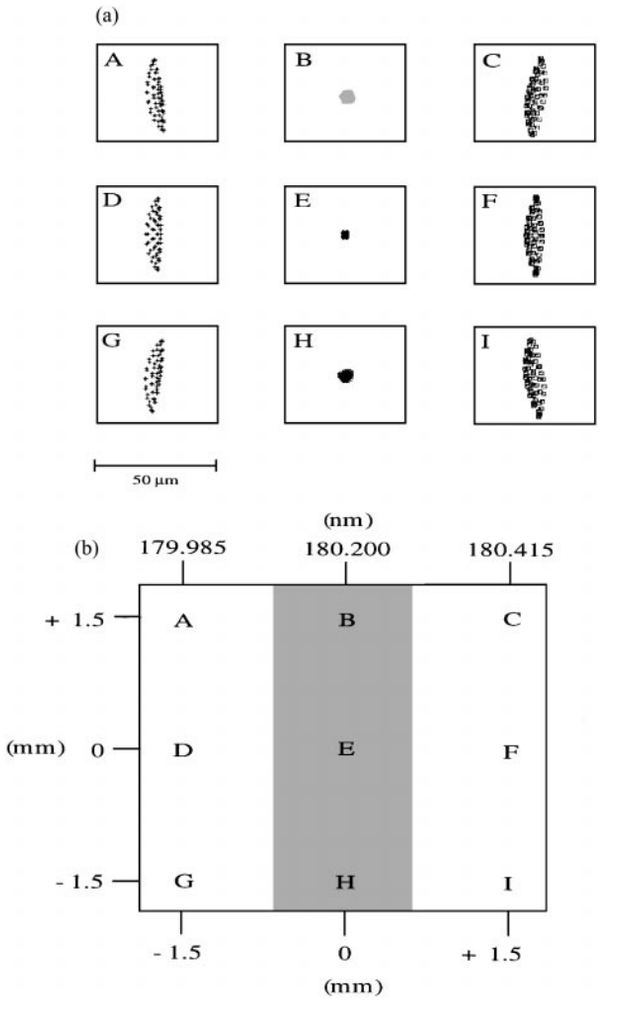

Fig. 3 (a) Spot diagrams for rays falling distributed on the focal plane of the echelle monochromator. (b) Represents an outline of the detector area at the focal plane. The locations on the focal plane of the spots depicted in (a) are shown on the detector outline. The shaded area indicates the 60 central pixels of the detector which are typically used for analytical measurements. The upper scale indicates the wavelength interval at 180 mm.

length of relatively high slits. Fig. 3 shows the result of a ray trace analysis carried out throughout the region of the grating monochromator focal plane which is covered by the detector. It can be seen that the blur radius increases only slightly at the top and bottom of a 3 mm slit image. The slit image curvature indicated by the centroids of the distributions results in only minor degradation when a 30 μm entrance slit is used. At the horizontal extremes, blurring becomes asymmetrical. In the direction of grating dispersion, the image degrades only slightly, but more so in the vertical. The absolute distortion is, however, small compared to the 3 mm slit height and of no analytical significance since the plasma emission intensity distribution is integrated. In practice, a spectral viewing range of about 60 pixels is usually selected in order to measure analyte and background emission. This corresponds to a spatial range of ± 0.504 mm about the center of the focal plane. The images throughout this range are essentially those shown in Fig. 3 for positions B, E and H.

The diffraction efficiency of the echelle gratings, ruled at Perkin Elmer West Coast Optics (Irvine, CA, USA), has been shown to peak at between 45–65% and at the same angle in all orders.[7] However, as the angular width of the free spectral range decreases with increasing order (Fig. 2), the efficiency drops rapidly for wavelengths diffracted away from the blaze maximum. For this reason, the blaze angle was adjusted during

the replication procedure from the ruling angle of 63.4° to 63.8°. This angle was selected in order to minimize angular differences between angle of diffraction and blaze angle for a number of important lines in the low UV, where radiation throughput is of particular importance. For example, the angular difference between the angle of diffraction and the 63.4° blaze angle is approximately 0.5° for the selenium 196.026 nm line in both orders 115 and 116. Thus the radiation energy is split approximately equally between the corresponding two grating positions. If the blaze angle is adjusted to 63.8, and selenium is measured in the 116th order, the angular difference is only 0.1° and the measured intensity is increased by a factor of two.

The spectral luminosity of the double monochromator, calculated as described in ref. 7 according to

$$L_\lambda = h(HW)\cos\ \phi\ \sin\ \beta/f\lambda \qquad (12)$$

where h is the entrance slit height, f the input collimator focal length, H and W the height and width of the echelle grating, respectively, and ϕ, the half angle between the incident and diffracted ray at the echelle, is 0.32 $mm^2\ nm^{-1}$ at 200 nm which, due primarily to the unrestricted height of the entrance slit (H), is about an order of magnitude higher than the values given in Table III of ref. 7.

A 30° prism made of calcium fluoride with an aluminized back surface is used in the pre-disperser. This material was selected due to its superior VUV transmission characteristics. Whereas 5 mm thick suprasil typically transmits only 20% at 165 nm (including 4% reflective losses at each of two surfaces), the same thickness of calcium fluoride transmits 87%. This is particularly important since, in the Littrow arrangement, radiation passes through the prism twice resulting in an effective average path length of 30 mm. The prism is used at an angle of incidence of 45.89° at 546 nm and is rotated by 4.37° in order to pass radiation at 167 nm through the slit. The complete range of rotation required to cover the wavelength region from 165 to 900 nm is ±2.38°. The rotation of both dispersive devices is accomplished simultaneously by 5-phase stepping motors with 2000 steps per revolution driving 1 mm pitch screws and operated at up to 10 KHz. Each step corresponds to 8.52×10^{-5}° and 1.24×10^{-4}° of rotation for the grating and prism, respectively. Since the motors are operated simultaneously, the theoretical maximum time required to select any wavelength between 167 and 900 nm is that required to rotate one dispersive element by 4.6°, *i.e.*, 3 s. In practice, lines are sorted according to wavelength, reducing overall travel, and the average selection time is of the order of 1 s, including the time allowed for mechanical settling before the start of measurement.

Dynamic wavelength stabilization

The spectrometer is equipped with a temperature sensor mounted on the prism. The measurement is representative of the ambient temperature within the spectrometer body and is used primarily to correct for the effects of temperature on the prism spectrum. The refractive index of CaF_2 has a temperature dependence as described by Malitson[22] which affects the angle of refraction for all wavelengths. Moreover, changes in temperature affect all components through thermal expansion, in particular that of the levers transferring the rotation of the lead screw to the rotation of the prism. This behaviour is reproducible and predictable so that a single, empirically derived, correction factor can be effective for all monochromators of the same design. An error in the position of the prism section does not affect wavelength accuracy but rather the transmitted intensity changes, if the magnitude of the error is such that the image of the entrance slit for a given wavelength no longer completely overlaps the intermediate slit. In order to assure intensity stability over a large operating temperature range, provision is made for automatic measurement and correction of prism positioning errors when a predefined temperature change is detected by the sensor.

First order corrections can also be made for the position of the grating, based on the effects of thermal expansion on grating groove spacing and on the grating lever arm. However, the accuracy of these corrections is by no means adequate for the wavelength assignment stability essential to ICP-OES. In this design, use is made of the characteristics of the double monochromator to achieve exact on-line correction of grating positioning changes for each measurement.[23]

The intermediate slit, which is at the same time the entrance slit of the echelle spectrometer, is divided into two vertical sections, as shown in Fig. 4. A reference spectrum from a neon low pressure discharge lamp is transmitted through a 0.5 mm plastic optical fiber onto the lower section of the intermediate slit. All wavelengths emerging from the fiber reach the echelle grating with no pre-selection, whereupon all diffraction orders are superimposed on the exit plane. The resulting spectrum is recorded on a section of the detector during the 'pre-shot' phase of each analytical measurement. This phase consists of a brief measurement of analyte emission intensity and is needed in order to determine the ideal integration time for the actual analytical measurement.

The superposition of all orders of the neon spectrum means that, for any grating position, the detector measures a well defined pattern of reference spectral lines. Each measured peak corresponds to a spectral line of neon, most of which have very well documented wavelengths. The pixel positions of the intensity peaks on the detector are compared with a table of peak locations generated individually and stored in the memory of each spectrometer. The angle of diffraction, and hence the position of each spectral line is calculated making use of eqn. (10) and this angle is compared with that calculated for the analytical spectral line of interest. The difference in angles combined with the focal length yields the difference in position at the detector. From the difference between the expected and measured positions of the neon spectrum on the detector, the number of grating steps required to correct for drifts and mechanical tolerances are calculated and applied before the actual analytical measurement begins. The corrected reference spectrum is recorded simultaneously with each actual measurement so that, effectively, a wavelength scale can be appended to the spectral intensity data for each measurement.

An environmental chamber, Model 38 RB/+10...+50IU (Weiss Umwelttechnik GmbH, Reiskirchen, Germany) providing a wide range of controlled ambient conditions was used to investigate the thermal stability achieved by the above means.

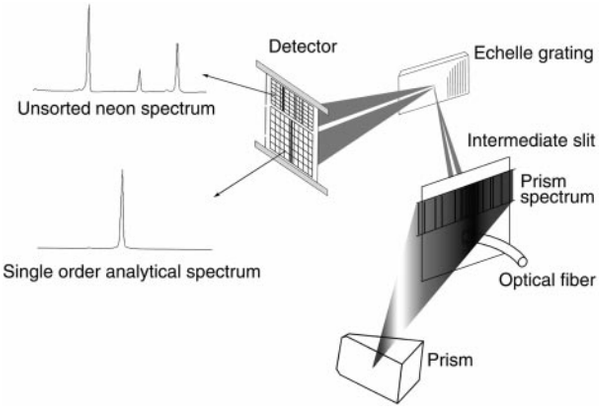

Fig. 4 Schematic of the arrangement for the simultaneous measurement of a neon reference spectrum. The spectrum is inverted in the grating monochromator so that the reference spectrum is measured using the upper section of the detector.

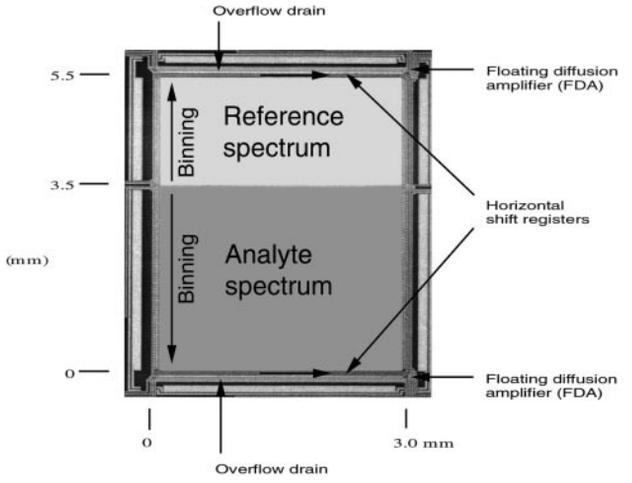

Fig. 5 Schematic diagram of the dual CCD detector. The sensitive area has a thickness of less than 20 μm.

Detector design

The detector is a two-dimensional back illuminated full frame transfer CCD array designed and manufactured by Hamamatsu Photonics K.K., (Hamamatsu City, Japan). The detector, depicted schematically in Fig. 5, contains 192 horizontal pixels each 18 μm wide of which 176 are exposed, resulting in a total width of 3.168 mm. This corresponds to a spectral interval of 0.436 nm at 167 nm and 2.09 nm at 800 nm. The unexposed pixels are used for the exact correction of electronic offsets. Vertically, the detector consists of two separate CCDs each with its own horizontal register. Each CCD has 64 vertical pixels. The lower section with horizontal register at the bottom is used to measure the analytical spectrum as a 1 : 1 image of the intermediate slit and has an overall height of 3.2 mm. The slit used for the reference spectrum is 0.5 mm high and is imaged on the 2 mm high upper section of the detector. The spectra are separated by 1 mm, minimizing optical crosstalk. Vertical as well as horizontal resolution can be obtained using the two-dimensional array. For the most part, however, analytical measurements are made using the two detector sections as linear CCD arrays by means of binning. In this mode the charge contained in all pixels is shifted vertically to the horizontal register before being shifted horizontally for readout. The specifications for the detector are given in Table 2.

The basic structure of a CCD consists of gate electrodes, an oxide layer and semiconductor layers. An n-type epitaxy layer about 20 μm thick is grown on a p-type silicon substrate. This 'buried channel' is separated from the electrodes by 20 nm thick layers of silicon dioxide and silicon nitride. The electrodes are made of polycrystalline silicon highly doped with boron. The quantum efficiency of the device depends on the absorption of photons in the silicon with sufficient energy to produce a photoelectron and on the collection of photoelectrons in the buried channel in potential wells formed under the gates corresponding to individual pixels.

Table 2 CCD detector specifications

Reference array	64 × 176 pixels, 18 × 32 μm
Analyte array	64 × 176 pixels, 18 × 56 μm
Full well capacity	
Vertical	500 000 electrons
Horizontal	1 100 000 electrons
Vertical binning rate	800 kHz
Horizontal shift-out rate	800 kHz
Horizontal read-out rate	125 kHz
CCD node sensitivity	2.2 μV per electron
Readout noise	15 electrons RMS
Photo response non-uniformity	<10%
Dark current (MPP mode)	120 electrons per pixel s^{-1} at −8 °C

The absorption of short wavelength photons by silicon is such that, in a conventional design, essentially no photons with wavelength shorter than 400 nm penetrate into the buried channel. One way to overcome this problem has been to coat the electrode surface of the CCD with a phosphor in order to convert UV photons into visible photons.[24] A more sophisticated approach is the use of virtual gates, applied very successfully in a segmented CCD consisting of linear arrays distributed at areas of interest in the focal plane of an echelle spectrometer.[17] The height of pixels to which this approach can be applied is limited, however, to about 200 μm. In order to make use of the full available slit height of the present echelle monochromator, a 2-dimensional CCD is used in binning mode as a linear array with pixels 3 mm long. The approach to increasing quantum efficiency taken in the current design is to remove the substrate from the back of the detector by chemical etching and to illuminate the epitaxy layer directly from the rear.[25,26] Crucial to the responsivity of the resulting detector is the efficiency with which photoelectrons produced very near to the back surface are collected in the buried channel. Immediately after the thinning process, there is a high positive charge density at the surface which traps most photoelectrons at the surface until they recombine. By means of an optimized combination of ion implantation and thermal annealing in a high temperature furnace,[27] a negative internal potential is generated at the back surface so that charges are driven to the buried channel as depicted in Fig. 6. Thereafter a silicon dioxide layer is thermally grown on the surface. The combination of collection efficiency and anti-reflection properties determines the quantum efficiency over a wide wavelength range. An additional advantage of backside illumination is that opaque aluminum can be used as electrode material, reducing electrical resistance as compared to that of polysilicon and thereby increasing possible clocking speeds.

The dark current is reduced by means of multi pinned phase (MPP) operation[28] by an order of magnitude, making cooling to about −8° sufficient for performance in the VUV. This level of cooling is achieved by means of a single stage Peltier element integrated into the detector package. Since only the mass of the CCD chip itself must be cooled, the dissipated power is only about 2.5 W for cooling to 40° below ambient, for which heat removal by forced air is sufficient. Another advantage of this design is that the cooled components are contained in a hermetically sealed package filled with dry nitrogen which insulates sufficiently so that the quartz window is at ambient temperature and there is no danger of condensation.

The CCD structure is designed with potential barriers between vertical pixel columns such that excess charge generated in any pixel within the sensitive area will overflow only in the vertical (binning) direction. Thus, the spectral

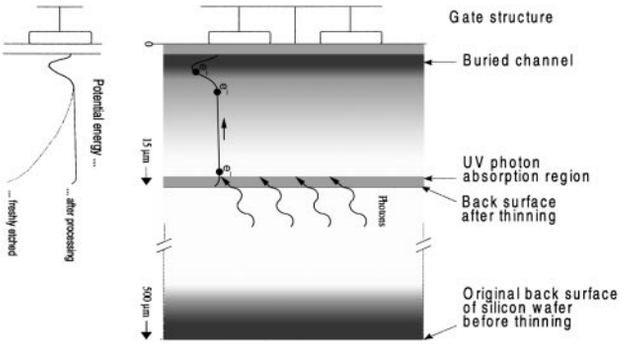

Fig. 6 Representation of the back illumination principle.

information content is not affected. Upon binning, the charge is transferred to horizontal register pixels, which are each equipped with lateral overflow drains (Fig. 5). An implant between the buried channel and the drain creates a potential barrier, the height of which is controlled by an overflow gate. The height of the overflow drain barrier is maintained lower than that of the barrier between pixels so that excess charge flows preferentially into the drain rather than into adjacent pixels.

The control and data acquisition electronics for the spectrometer employs a combination of of timing RAM and FPGA (field programmable gate array) for flexible readout of the two detector sections. Whereas the entire neon spectrum is recorded for each measurement, only a user specified section of the analytical spectrum is acquired. Correlated double sampling circuitry[29,30] is used to reduce kTC and $1/f$ amplifier noise. The circuitry also contains provision for pulsed operation of an LED used in detector tests and for synchronization of the neon lamp output with reference spectrum integration.

Fundamental measurements of spectrometer properties were made using hollow cathode (HCL) and electrodeless discharge (EDL) lamps from Perkin Elmer as well as a high pressure mercury arc lamp (Osram GmbH, Munich, Germany, Model HG/100) and the built-in neon reference lamp (Jelight Inc, Irvine, CA, USA; Model 78-Neon-1SMT). Analytical OES measurements were made using the apparatus and conditions listed in Table 3.

Standard solutions were made by appropriate dilution of single or multielement standards (Merck, Darmstadt, Germany) in 0.2% nitric acid.

Results and discussion

Detector characteristics

The photon transfer function of a radiation detection system defines the relationship between photocharge and output signal.[31] A series of measurements were carried out at varying photocharge levels. In each case, the digital values obtained for a pair of identical measurements were subtracted pixelwise in order to eliminate the effect of pixel-to-pixel non-uniformity. The measured standard deviation of the readings for 176 pixels was divided by two and plotted against the signal magnitude. In the region where shot noise dominated, the measured standard deviation increased with the square root of signal. The overall gain in electrons per digit was calculated from the slope of the plot of signal variance *vs.* signal. The measured gain, 6 electrons per digit, when converted using the total electronic amplification factor and expressed in μV per electron at the output of the CCD's floating diffusion amplifier, gives a value of 2.3 μV per e^-, which is in good agreement with the specification. The measured readout noise of 4.5 digits (27 electrons) includes that of the detector amplifier, the electronics and of quantization.

The quantum efficiency (QE), defined as 100 times the ratio between incident photons and collected photoelectrons is of particular importance in the wavelength range where the plasma background intensity is low. The higher the efficiency, the higher the ratio between plasma background and detector dark current shot noise and the shorter the time required to collect a given number of photoelectrons. The QE in the low UV and VUV was measured using an Acton Research VM505 vacuum monochromator and United Detector Technology 7494 photodiode calibrated by NIST as described in ref. 17. At longer wavelengths, a Nikon AS-D102 scanning monochromator equipped with deuterium arc and halogen sources was used with a reference diode (Hamamatsu S1227-1010BQ) having a calibration traceable to NIST.

QE was calculated for each measurement wavelength by comparing the number of photoelectrons generated per unit time in the CCD and the photodiode for the same illumination. This yielded the curve shown in Fig. 7. The backside thinning and surface conditioning process results not only in efficiency approaching 100% in the visible range but also better than 50% throughout the key low UV range. Interestingly, quantum efficiencies greater than 100% can be measured as also reported previously[17] at wavelengths where photons are energetic enough to produce multiple hole–electron pairs.[31] The detailed form of the curve is a combination of the effects of dielectric anti-reflection coatings, absorption depth and efficiency of collection in the buried channel.

The average dark current for a sample of 20 detectors was measured to be 34 electrons per pixel s^{-1} at −8 °C. Since dark current doubles for every 7 degree increase in temperature, this corresponds to a specific dark current of less than 2000 electrons mm^{-2} at −40 °C. The advantage of MPP operation becomes evident when this value is compared with those reported for conventionally operated CCDs which are typically between 5×10^4 and 10^5 electrons mm^{-2} at −40 °C. Individual pixel fluctuations are not important since the detector is used in binning mode for analytical measurements. The average dark current for the 18×3200 μm 'pixels' is 2176 electrons s^{-1}. The average total read-out noise of 27 electrons corresponds to the dark current noise for 729 electrons dark current, *i.e.*, a measurement time of 0.33 s.

To determine response linearity, the detector was diffusely illuminated by an Opto Devices 333-UWC LED source. The integration time was held constant and sequences of uniform 1 μs pulses were applied to the LED using the spectrometer electronics. The total number of photons reaching the detector was directly proportional to the number of pulses in the integration interval. The measured response was effectively constant over most of the digital measurement range with no systematic deviation from linearity. The total response stopped increasing and the response per pulse dropped to zero only when the 16 bit range (65 535 counts) was exceeded. The linear range covered for any given single integration is given by 60 000/4.5 = 13 333 or more than four orders of magnitude. The shortest integration times are determined by the minimum time required to bin vertical pixels and shift out the horizontal

Table 3 ICP conditions

Sapphire-tipped cross-flow nebulizer, Scott spray chamber	
Solid state, 40 MHz generator, rf power 1300 W	
Plasma flow	15 L min^{-1}
Auxiliary flow	0.2 L min^{-1}
Nebulizer flow	0.8 L min^{-1}
Sample flow rate	1.50 mL min^{-1}
Viewing height (radial)	15 mm above load coil

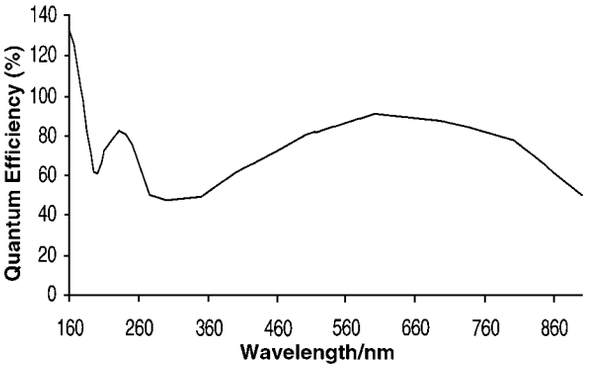

Fig. 7 Plot of quantum efficiency *vs.* wavelength measured for the back illuminated CCD using a reference photodiode and vacuum monochromator.

register, *i.e.*, 330 μs. The longest single integration is limited by the 16-bit counter to 8 s. This, together with the possibility for attenuation by a factor of 50 using the shutter wheel, provides a dynamic range for the measurement of any given sample of 1.6×10^{10}. Based on the 'pre-shot' intensity estimation, integration times and attenuation conditions are calculated such that approximately 30 000 counts are generated per individual integration. For any selected total measurement time, the appropriate number of replicate integrations are made and averaged automatically by the microprocessor of the spectrometer before the spectral data is transferred to the controlling PC.

Stray light

In echelle spectrometers with internal cross dispersion, the spectrum of interest is dispersed in two dimensions at the focal plane. Diffuse reflections from optical components and housing surfaces result in a level of background illumination which is proportional to the total intensity of the entire spectrum. This is measured as plasma background increasing the photon shot noise in the measurement and hence the limit of detection. Very bright lines, such as the 393.3 nm calcium line, can produce radiation fluxes as much as 10 orders of magnitude higher than that of plasma background in the low UV, when the interfering element is present at high concentrations. It has been shown that there is a slight but significant deterioration of detection limit with increasing calcium concentration even in a well-designed polychromator system.[7]

The use of a double monochromator to perform 'external cross-dispersion', *i.e.*, to permit only a small spectral bandwidth to enter the grating monochromator, has the advantage that the potential for generation of diffuse straylight is fundamentally limited. Only bright lines in the immediate vicinity of the analyte line can be scattered. Other lines enter the grating spectrometer attenuated by a factor which depends on the quality of stray light rejection in the preselecting monochromator. As an example, the effect of a 10 000 mg L^{-1} Ca solution on the baseline near the arsenic line at 193.696 nm is shown in Fig. 8. Based on the signal for 1 mg L^{-1} arsenic, the change in the baseline due to calcium is calculated to be equivalent to 75 μg L^{-1} arsenic and the effect on detection limit is negligible.

The key to the overall straylight performance is the efficiency with which the prism monochromator rejects radiation outside of the selected wavelength range. Any unwanted radiation entering the grating monochromator is dispersed by the grating and detected with no further order sorting. Great care was therefore taken in the design of baffles and the elimination of multiple refractions. The latter occur in all in-plane monochromator designs when wavelengths other than those of interest can follow a path to the exit slit.[32] Multiple refractions are reduced by means of horizontal masks 5 mm high located on both the parabolas and the dispersive components in the plane of the entrance and exit slits. The base angle of the prism was also tilted by 2° in order to direct internal reflections from this surface downward. The overall attenuation of unwanted radiation by the prism monochromator was measured for the 546.074 nm line emitted by a high pressure mercury arc lamp. The peak intensity was measured with the prism monochromator set to transmit the line, then the prism monochromator was rotated by 10 000 steps without moving the grating monochromator and the measurement was repeated. The attenuation, calculated as the ratio of intensities, was typically greater than 10^4.

The performance of the echelle grating, replicated from a master ruled by an interferometrically controlled engine, has been characterized.[7] The measured Rowland and Lyman ghosts are of essentially no analytical significance.

Thermal stability

The properties of all materials are affected to a greater or lesser extent by changes in temperature. Historically, in order to maintain acceptable wavelength calibration stability, high resolution spectrometers had either to be operated in very stable environments and/or built into sealed housings, which were maintained at a preset temperature, thermostatically controlled to within ≈0.5 °C. In the current design an active approach based on first order corrections for measured temperature changes and simultaneous measurement of a reference spectrum was taken.

The performance depends on the stability of the two monochromators in different ways. The convolution of entrance and intermediate slits results in a trapezoid. The width of the plateau depends on the slit widths and here is nominally 270 and 120 μm for the 300 and 150 μm entrance slits, respectively. Thus intensity stability is maintained provided that the position of the prism spectrum changes by less than this amount. The primary thermal effects on the position of the prism spectrum result from expansion of the wavelength drive components and the change in refractive index of the prism itself.

Fig. 9 shows uncorrected prism spectrum drift as a function of ambient temperature and residual drift after empirical correction. It is evident that, when the 300 μm intermediate slit

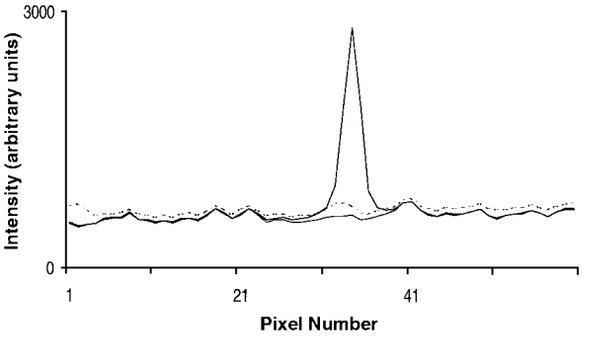

Fig. 8 Diffuse stray light from a 10000 mg L^{-1} Ca solution near 193 nm. Signals for 1 mg L^{-1} As at the 193.696 nm line (——), dilute nitric acid blank (-----) and 10 000 mg L^{-1} Ca (·····). Measurements were made under the plasma conditions listed in Table 3, all with 1 s integration time.

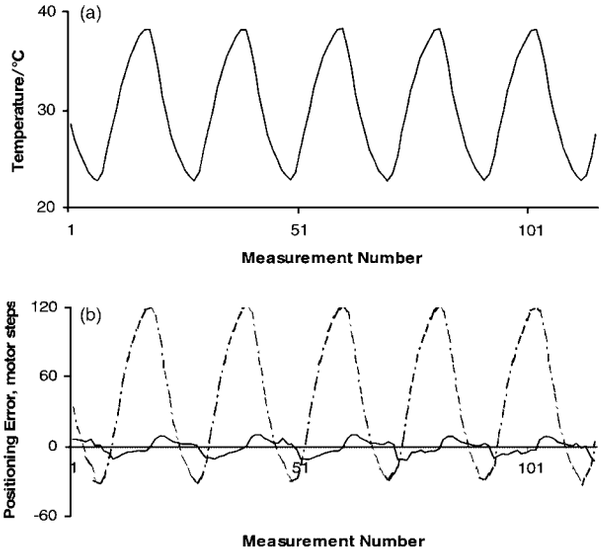

Fig. 9 (a) Internal temperature measured at the prism for several 15 to 35 °C ambient temperature cycles. (b) Effect of empirical correction on the positioning error for the prism measured over the temperature cycles shown in (a). Uncorrected position is shown dotted. (1 motor step ≈ 1.3 μm at the focal plane.)

is used, prism position does not affect measurements, whereas, for the narrower slit, the residual error for temperature changes greater than 7 °C may be significant. For this reason, the temperature sensor is used to automatically initiate a scan of prism position *vs.* intensity when this is required. In routine operation using an ICP source, the scans are carried out on two argon lines whenever temperature changes larger than 3 °C are detected and the appropriate correction to the calculation of prism drive motor position is made. Thus spectrometer throughput stability is guaranteed and the location of the prism spectrum is documented. Under normal ambient conditions, this measurement is activated only upon start up and at most once after warm up of the spectrometer.

A correction algorithm was developed in order to dynamically correct and document analyte spectral line position. The portion of the order-overlapped neon spectrum falling on the 3.16 mm detector width was recorded for each spectrometer at 200 motor step intervals. Fig. 10 shows a reference spectrum covering the entire range of grating rotation obtained by putting together individual segments all measured at an integration time of 5 ms. During the measurements for individual spectrometers, integration times were adjusted automatically for regions of low or high spectral intensity such that a useable reference spectrum was recorded throughout the range. A table of peak positions and integration times *vs.* motor position was generated and stored in the spectrometer permanent (FLASH) memory. For any given measurement, the firmware estimates the expected positions of reference peaks by interpolation. The grating position is then corrected by the difference between the measured and calculated neon line positions before the analytical measurement takes place.

The line center position was measured over a ± 10 °C temperature range cycled several times over a seventy hour period. The rms variation in the center of the intensity distribution was less than 0.06 pixel. This corresponds to a distance of 1.2 μm at the exit slit and a spectral shift of, for example, 0.0002 nm at 200 nm. This is 2.8% of the 0.007 nm fwhm (full width at half-maximum) spectral bandwidth of the monochromator at this wavelength.

The overall intensity stability of an ICP-OES spectrometer is a function of the transmission and wavelength stability of the spectrometer and the stability of the source. In order to isolate, as much as possible, the contribution of the spectrometer, stability measurements were made using an EDL for lead operated at nearly constant ambient temperature. The instrument was located in an environmental chamber and the radiation from the lamp was transferred to the spectrometer by means of an optical fiber bundle passing through the insulated wall of the chamber. One end of the bundle was placed at a 1 : 1 image of the EDL produced by a toroidal mirror and the other in place of the ICP torch at the image point of the axial channel of the spectrometer transfer optics. The intensity, calculated

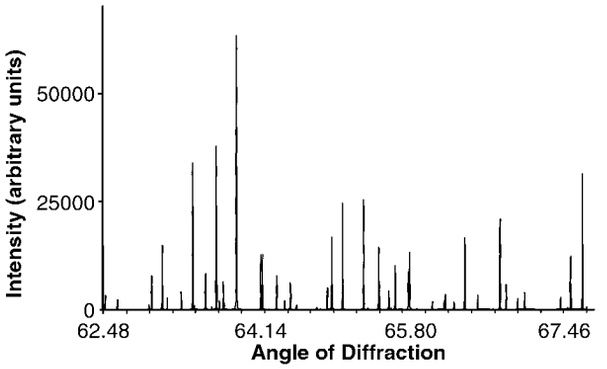

Fig. 10 The spectrum of the neon reference lamp as a function of angle of diffraction measured with 5 ms integration time.

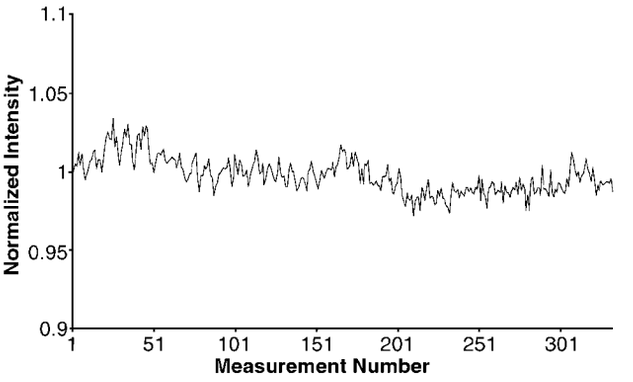

Fig. 11 The normalized intensity of the argon 420.610 nm line emitted from an EDL over a 5 day period during which temperature was cycled twice daily as in Fig. 9(a). Intensity was measured as the sum of six pixels with background correction by subtraction of 3 pixels on each side.

using 6 pixel peak area integration, with background correction, is plotted for the 70 hour period of the above measurement in Fig. 11. The intensity variations do not exceed $\pm 2\%$ over this extreme ambient temperature range.

Fig. 12 shows an overlay of all the 250 line profiles measured for the Ar line at 420 nm. As indicated by peak position data, the center of the profiles remains constant but, not unexpectedly, there is a change in the profile. This arises from a slight alteration of the focus of the slit image in the monochromator. The coefficient of expansion of aluminum is 23.9×10^{-6}.[33] Thus the optical base, measuring 300 mm between the slit and the parabola will expand by 7.2×10^{-3} mm per °C temperature change. At the same time, the optical glass (BK-7) of the parabola expands according to its coefficient of 7.1×10^{-6},[33] increasing the focal length of the mirror and partially compensating the expansion of the base. The net calculated result for the F/6 monochromator is a change in fwhm of about 8 μm for a 10 °C temperature change as experienced by the spectrometer components. This corresponds well to the measured behaviour shown in Fig. 13. The instrument is designed for operation within an ambient temperature range of from 15 to 35 °C. The spectrometer components mounted in the instrument housing experience a temperature range between 22 and 42 °C under these conditions. Accordingly, the spectrometer is focused for optimum performance at a nominal internal temperature of 32 °C so that the the defocusing effect is never more than that shown in Fig. 13.

Fig. 14 shows the thallium doublet at 190.8 nm emitted from an ICP source. The fwhm calculated based on the width and position difference of the doublet peaks is 6.8 pm. The measured half width depends on the physical line profile, slit width, optical aberrations, production tolerances and the

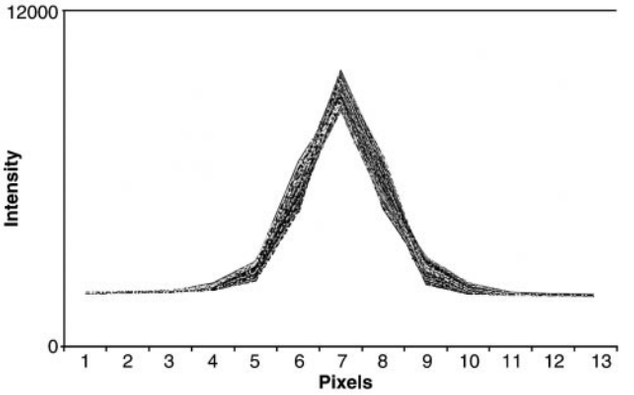

Fig. 12 Overlay of 250 line profiles measured for the argon line at 420.610 nm over the full range of temperatures as shown in Fig. 9(a).

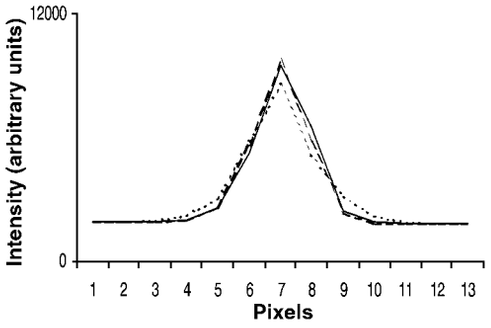

Fig. 13 Comparison of three line profiles for the argon line at 420.610 nm measured at extreme internal temperatures. The profiles were measured at 38 (——), 30.5 (-----) and 22.4 °C (·····).

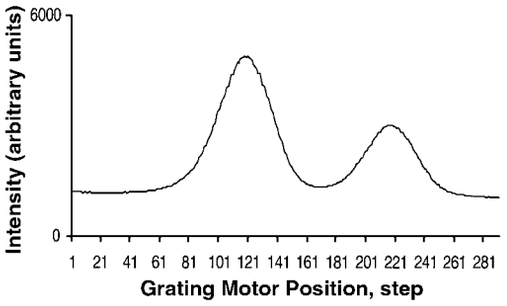

Fig. 14 Plot of relative intensity *vs.* grating position measured for the thallium doublet at 190.801 nm.

Table 4 Spectral bandpass *vs.* wavelength

Element	Wavelength/nm	Measured fwhm/nm
As	193	0.007
Ni	231	0.008
Ni	341	0.012
Ba	455	0.015
Li	670	0.023

modulation transfer function (MTF) of the detector. In backside illuminated detectors, the gate electrodes, which define the potential wells for each pixel, are located on the detector surface opposite to that at which photoelectrons are generated. In particular, the depth of penetration for photons with wavelengths in the vicinity of 200 nm is only a few nanometers, so that charge is generated at the surface only. For this reason, the thickness of the silicon layer remaining after thinning must be of the order of the pixel width. The predicted image width for a 30 μm slit, taking into account aberrations and expected production tolerances is 37 μm. The measured profiles in Fig. 13 demonstrate that detector MTF makes only a

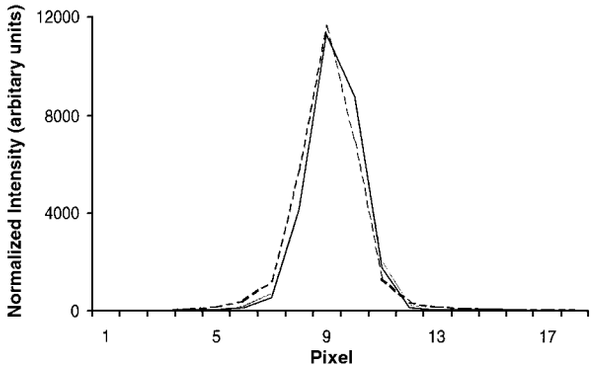

Fig. 15 Overlay of line profiles measured at 197 (——), 346 (-----) and 643 nm (·····) using EDL lamps.

minimum contribution to the measured image. The uniformity of the line profiles for lines between 190 and 850 nm overlayed in Fig. 15 confirm this, since longer wavelength profiles would be expected to be less affected by excessive detector thickness. Thus the overall image quality is uniform throughout the range of the spectrometer and spectral bandpass is dependent only on linear dispersion through the number of the diffraction order as summarized in Table 4 for a series of measurements made using EDL lamps.

The optical performance of the spectrometer system applied to ICP-OES was evaluated by making a series of characteristic ICP spectral measurements. Viewing positions in both axial and radial modes had been optimized based on the intensity of the manganese spectral line at 257.610 nm. The apparatus and conditions for the measurements were as listed in Table 3. Tables 5 and 6 show results for plasma background and analyte signal intensities as well as calculated and measured detection limits for a series of representative, analytically significant spectral lines.

The radiation throughput of the present system is so high that source flicker noise dominates shot noise throughout almost the entire wavelength range. Comparison of the columns labelled '5 s BGC' (background correction) and '5 s Peak' in Tables 5 and 6 shows that lower detection limits are measured without background correction only for wavelengths below about 200 nm for axial viewing and 230 nm for radial viewing. The background correction was based on the average of 2 selected pixels. According to previous reports,[15] still better results could be obtained using MSF (multicomponent spectral fitting) data processing because the algorithm makes use of all the points within a selected wavelength region, thereby reducing the variance of the background estimate by the number of measurement points. The MSF approach is also invaluable in cases of complex background. However, the simple method of background correction used here was sufficient to illustrate the benefit of simultaneous detection in

Table 5 Comparison of calculated and measured detection limits for axial viewing

					Detection limit (3σ)/μg l^{-1}			
Element	λ/nm	Z_b/e^- pixel^{-1} ms^{-1}	S/e^{-1} s^{-1} μg^{-1} l	BEC/μg l^{-1}	Calculated 5 s BGC	Measured 5 s BGC	Measured 5 s peak	Measured 50 s BGC
P	177.434	2.5	72	106	3.5	3.0	2.4	2.1
Tl	190.801	12.3	192	193	2.3	2.2	1.6	0.8
As	193.696	12.3	156	236	2.8	2.3	3.6	0.9
Se	196.026	14.2	158	268	3.0	2.7	2.1	0.8
Zn	213.857	48.1	6650	22	0.12	0.16	0.3	0.04
Pb	220.353	52.7	469	337	1.8	1.5	2.8	0.5
Cd	226.502	61.4	6867	26	0.13	0.16	0.25	0.05
Mn	257.610	174	49046	11	0.03	0.03	0.12	0.01
V	292.402	240	9444	76	0.19	0.25	0.41	0.24
Cu	324.752	551	15425	107	0.18	0.28	0.71	0.23
Li	670.784	779	10205	24	0.02	0.05	0.16	0.01

Table 6 Comparison of calculated and measured detection limits for radial viewing

Element	λ/nm	Z_b/e$^-$ pixel^{-1} ms^{-1}	S/e^{-1} s^{-1} μg^{-1} l	BEC/μg l^{-1}	Detection limit (3σ)/μg l^{-1}			
					Calculated 5 s BGC	Measured 5 s BGC	Measured 5 s peak	Measured 50 s BGC
P	177.434	0.82	12	202	16.5	12.3	8.1	12.6
Tl	190.801	3.9	30.5	379	9.4	8.5	7.2	2.9
As	193.696	3.0	31.4	282	8.4	9.3	5.7	2.7
Se	196.026	3.9	26.9	434	10.6	8.1	6.8	2.4
Zn	213.857	5.8	1302	13	0.25	0.3	0.3	0.09
Pb	220.353	15.5	78	597	6.3	5.7	7.5	1.2
Cd	226.502	18.9	1103	51	0.48	0.5	0.3	0.1
Mn	257.610	50.2	6505	23	0.13	0.1	0.3	0.03
V	292.402	71.2	1170	183	0.85	0.5	0.9	0.4
Cu	324.752	128.2	1596	241	0.83	0.7	2.5	0.2

eliminating wavelength-correlated source flicker noise as, for example, in the case of the determination of copper at 324 nm.

Due to the very low dark current level resulting from MPP operation, the detector characteristics are well matched to the spectrometer. If the detector noise contributions are set to zero in the theoretical calculation, there is a significant improvement (greater than a factor of 1.5) in detection limits only at wavelengths shorter than 180 nm. Thus the added complexity of a second peltier stage and/or water cooling for the reduction of dark current would have little analytical benefit and would not be justified. The detector readout noise is not a factor in any case.

As can be inferred from Tables 5 and 6, the high photon collection and conversion efficiency of the present system minimizes the time required to obtain state of the art detection limits. The total time required for measurement at twenty element lines each with 1 s integration time and including wavelength setting and pre-shot for automatic wavelength correction and integration time optimization was determined to be about 75 s.

Acknowledgements

The authors would like to thank Klaus Fischer, Günther Dencks and Bernd Vögtle for contributions to the development of the spectrometer and Paul Krampitz, Susan McIntosh, Joachim Nölte and Michael Sperling for assistance in the evaluation. Critical reading of the manuscript by Daniel Gordon and Dennis Yates is gratefully acknowledged. Special thanks are due to Tiezheng Guo for providing many of the analytical results and to Stephen Helliwell for preparing the drawings.

References

1 W. N. Hartley, *J. Chem. Soc.*, 1882, **41**, 210.
2 A. de Gramont, *Rev. Met.*, 1922, **19**, 90.
3 A. N. Zaidel, V. K. Prokofjev, S. M. Raiskii, V. A. Slavnyi and E. A. Shreider, *Tables of Spectral Lines*, IFI/Plenum, New York, 1970.
4 G. L. Clark, in *The Encyclopedia of Spectroscopy*, ed. G. L. Clark, Reinhold Publishing Corporation, New York, 1960.
5 V. Karanassios and G. Horlick, *Appl. Spectrosc.*, 1986, **40**, 813.
6 M. J. Pilon, M. B. Denton, R. G. Schleicher, P. M. Moran and S. B. Smith Jr., *Appl. Spectrosc.*, 1990, **44**, 1613.
7 T. W. Barnard, M. I. Crockett, J. C. Ivaldi and P. L. Lundberg, *Anal. Chem.*, 1993, **65**, 1225.
8 J. M. Harnly, *J. Anal. At. Spectrom.*, 1999, **14**, 137.
9 P. S. Doidge and T. T. Nham, *Appl. Spectrosc.*, 1992, **46**, 1301.
10 P. N. Keliher and C. G. Wohlers, *Anal. Chem.*, 1976, **48**, 333A.
11 G. H. C. Freeman, M. Outred and L. R. Morris, *Spectrochim. Acta, Part B*, 1980, **35**, 687.
12 P. W. J. M. Boumans and J. J. A. M. Vrakking, *Spectrochim. Acta, Part B*, 1984, **39**, 1239.
13 U. Heitmann, M. Schütz, H. Becker-Ross and S. Florek, *Spectrochim. Acta, Part B*, 1996, **51**, 1095.
14 B. Sierk, S. Florek, H. Becker-Ross, B. Bürki, L. Kruse and H.-G. Kahle, Astrophysical Research Abstracts, 1999, **1**(1), OA22.
15 J. C. Ivaldi, D. Tracy, T. W. Barnard and W. Slavin, *Spectrochim. Acta, Part B*, 1992, **47**, 1361.
16 P. W. J. M. Boumans, *Spectrochim. Acta, Part B*, 1991, **46**, 431.
17 T. W. Barnard, M. I. Crockett, J. C. Ivaldi, P. L. Lundberg, D. A. Yates, P. A. Levine and D. Sauer, *J. Anal. Chem.*, 1993, **65**, 1231.
18 G. R. Harrison, *Appl. Opt.*, 1949, **12**, 522.
19 D. Schröder, *Publ. Astron. Soc. Pac.*, 1970, **82**, 1253.
20 S. Florek and H. Becker-Ross, *J. Anal. At. Spectrom.*, 1995, **10**, 145.
21 A. Walsh, *Nature*, 1951, **167**, 810.
22 I. H. Malitson, *Appl. Opt.*, 1963, **2**, 1103.
23 H. Becker-Ross, S. Florek and B. Radziuk, *Ger. Pat.*, DE 19545178, 1995.
24 G. R. Sims, in *Charge-Transfer Devices in Spectroscopy*, ed. J. V. Sweedler, K. L. Ratzlaff and M. B. Denton, VCH Publishers, Inc., New York, 1994.
25 J. Janesick, T. Elliot, T. Daud, J. McCarthy and M. Blouke, *Proc. SPIE*, 1985, **570–78**, 46.
26 M. P. Lesser, in *Recent Developments in Scientific Optical Imaging*, eds. B. Denton, R. E. Fields and Q. S. Hanley, Royal Society of Chemistry, Cambridge, 1996.
27 M. Muramatsu, H. Akahori, K. Shibayama, S. Nakamura and K. Yamamoto, *SPIE*, 1997, **3019**, 2.
28 J. Janesick, T. Elliot, G. Fraschetti, S. Collins, M. Blouke and B. Corrie, *Proc. SPIE*, 1989, **1071–15**, 153.
29 D. Barbe, *Proc. IEEE*, 1975, **63**, 38.
30 J. Janesick, T. Elliot, S. Collins, M. Blouke and J. Freeman, *Opt. Eng.*, 1987, **26**, 692.
31 J. Janesick, K. P. Klaasen and T. Elliot, *Opt. Eng.*, 1987, **26**, 972.
32 J. K. Pribham and C. M. Penchina, *Appl. Opt.*, 1968, **7**, 2005.
33 *CRC Handbook of Chemistry and Physics*, ed. D. R. Lide, 72nd edn., CRC Press, Boca Raton, FL, 1994.